

# Tracing Multi-scale Magnetic Field Structure Using Multiple Chemical Tracers in Giant Molecular Clouds

Yue Hu<sup>1,2</sup>, Ka Ho Yuen<sup>1</sup>, A. Lazarian<sup>1</sup>, Laura M. Fissel<sup>3</sup>, P. A. Jones<sup>4</sup>, and M. R. Cunningham<sup>4</sup> Department of Astronomy, University of Wisconsin–Madison, Madison, WI, USA; yue.hu@wisc.edu

Department of Physics, University of Wisconsin–Madison, Madison, WI, USA

National Radio Astronomy Observatory, Charlottesville, VA, USA

School of Physics, University of New South Wales, Sydney, NSW 2052, Australia

Received 2019 April 3; revised 2019 September 3; accepted 2019 September 4; published 2019 October 18

#### **Abstract**

Probing magnetic fields in giant molecular clouds is often challenging. Fortunately, recent simulations show that analysis of velocity gradients (the velocity gradient technique; VGT) can be used to map out the magnetic field morphology of different physical layers within molecular clouds when applied to CO isotopologues with different optical depths. Here, we test the effectiveness of the VGT in reconstructing the magnetic field structure of the molecular cloud Vela C, employing seven chemical tracers that have different optical depths, i.e., <sup>12</sup>CO, <sup>13</sup>CO, Clad, CS, HNC, HCO<sup>+</sup>, and HCN. Our results show good correspondence between the magnetic field morphology inferred from velocity gradients using these different molecular tracers and the magnetic field morphology inferred from BLASTPol polarization observations. We also explore the possibility of using a combination of velocity gradients for multiple chemical tracers to explain the structure of the magnetic field in molecular clouds. We search for signatures of gravitational collapse in the alignment of the velocity gradients and magnetic field and conclude that collapsing regions constitute a small fraction of the cloud.

Key words: ISM: general – ISM: structure – radio lines: ISM – turbulence

#### 1. Introduction

The magnetic field in the universe plays an essential role in multiple astrophysical processes, e.g., regulation of star formation (Chapman et al. 2013; Burkhart et al. 2015), guiding material and thermodynamic transfer between different media, and propagation and acceleration of cosmic rays (Fermi 1949; Caprioli & Spitkovsky 2014). One of the most critical roles of the magnetic field is to modify the ubiquitous interstellar turbulence (Mac Low & Klessen 2004; Ballesteros-Paredes et al. 2007) both in the diffuse interstellar medium (ISM), e.g., neutral hydrogen (H I), and in molecular gas (Bell & Lin 1994; Ostriker et al. 2001; Heitsch et al. 2007) which is distributed over an extensive range of density regimes in galaxies. While most of the sightlines toward giant molecular clouds (GMCs) have low column density  $(\leq 10^{22} \,\mathrm{cm}^{-3})$ , it is the properties of the dense gas components, such as magnetic field strength, turbulent energy, and angular momentum, that regulate the region where new stars are being born (Li et al. 2005; Leroy et al. 2008; Murray et al. 2010; Chen et al. 2015; Soler et al. 2017; Soler & Hennebelle 2017). Thus, an exploration of their contribution to the dynamical evolution of molecular clouds is crucial to fully understand the process of star formation (Solomon & Sage 1988; Gao & Solomon 2004; Hopkins et al. 2012).

Many methods of tracing the magnetic fields have been proposed, although each method has limitations and biases. For instance, measuring polarization from dust grain alignment (Lazarian 2007; Andersson et al. 2015; Planck Collaboration et al. 2015) requires high-sensitivity, large-scale far-infrared or sub-mm polarization maps, which are extremely time-consuming from ground-based telescopes and often have low dust grain alignment efficiency (Lazarian 2007). Surveys of magnetic fields from polarization due to the selective extinction of starlight passing through dust clouds are not highly effective for clouds with large dust columns. The synchrotron polarization method

(Carilli & Taylor 2002; Draine 2011; Jansson & Farrar 2012) is mostly used to trace the magnetic field in the warm and hot phases of the ISM, while, using Faraday rotation, one can only measure the magnetic field along the line of sight toward regions where the ionization is significant (Hill et al. 2013).

Both numerical simulations and observations have shown that the velocity gradient technique (VGT) is a promising method for studying magnetic fields (González-Casanova & Lazarian 2017 (henceforth GL17); Yuen & Lazarian 2017a (henceforth YL17); Lazarian & Yuen 2018b; Lazarian et al. 2018; Hsieh et al. 2019; Hu et al. 2019a, 2019b; Zhang et al. 2019). The first suggestion to use velocity gradients to trace magnetic fields was made in GL17 where velocity centroid gradients (VCGs) were used as proxies of velocity gradients. This technique was applied to a wide range of column densities from diffuse neutral hydrogen (H I) gas in YL17 and Hu et al. (2018), and later Lazarian & Yuen (2018b) proposed to use velocity channel gradients (VChGs) to trace magnetic fields. The application of these techniques to the diffuse H I data has proven the effectiveness of this radically new method of magnetic field study (Lazarian & Yuen 2018b). A recent exploration of the gradients technique in self-absorbing molecular gas data and self-gravitating media (Yuen & Lazarian 2017b; González-Casanova et al. 2019; Hsieh et al. 2019; Hu et al. 2019a, 2019b) have also demonstrated that the VGT can be used as a tracer of the magnetic field in regions with different physical conditions using <sup>13</sup>CO as a molecular tracer.

In this paper, we present an observational example for the low galactic latitude GMC Vela C using a recent enhancement of the VGT made by Hsieh et al. (2019) in numerical simulations, which demonstrated that VGT can also be applied to CO isotopologues including  $^{12}$ CO and  $^{18}$ O. We use seven molecular line maps for the analysis in Vela C, including the three isotopes of CO, CS, HNC, HCO $^+$ , and HCN. The last four molecular tracers are high-density tracers (number density of  $^{12}$ CO, around  $^{10}$ - $^{10}$ 6 cm $^{-3}$ 9 compared to the CO tracers  $^{12}$ CO,

 $^{13}\text{CO}$ , and  $\text{C}^{18}\text{O}$ , which typically trace number densities of  $\text{H}_2$  between  $10^2$  and  $10^4\,\text{cm}^{-3}$  (Shirley 2015; Fissel et al. 2019). To evaluate the success of the VGT we compare our inferred magnetic field orientation from the VGT to the magnetic field orientation inferred from a large-scale 500  $\mu\text{m}$  Balloon-borne Large-Aperture Sub-millimeter Telescope for Polarimetry (BLASTPol) polarization map first presented in Fissel et al. (2016).

In Sections 2 and 3, we describe the theoretical foundation and the VGT used in our work. In Section 4, we discuss the ability of the VGT to trace magnetic fields over a large range of densities in GMCs and the contribution from the foreground and background. In Section 5, we show how to trace the magnetic field through a combination of different molecular tracers and estimate the fraction of the collapsing regions in Vela C. In Section 6 we discuss the possible application of the VGT to other molecular clouds. In Section 7 we give our conclusions.

# 2. Theoretical Perspective on the Self-absorbing Gradient Technique

# 2.1. Basic Magnetohydrodynamic Turbulence Theory

Magnetohydrodynamic (MHD) turbulence has been explored both theoretically and numerically for decades (Shebalin et al. 1983; Higdon 1984; Montgomery & Matthaeus 1995). Goldreich & Sridhar (1995; henceforth GS95) formulated the theory of incompressible MHD turbulence and also predicted turbulent anisotropy, which later became the foundation of several magnetic field tracing techniques. GS95 showed that the scaling of turbulent eddies is approximately  $v_l \sim l^{\frac{1}{3}}$ , where  $v_l$  is the turbulence velocity at scale l and l is the size of eddies perpendicular to the magnetic field. However, GS95 did not address the mean magnetic field where the anisotropic relation is not expected to be observed.

Lazarian & Vishniac (1999) illustrated that the motion of turbulent eddies enables magnetic fields to mix with minimal resistance from magnetic tension for eddies at all scales and thus a much faster rate of magnetic reconnection is allowed compared to the traditional Sweet–Parker model. As a result of the mixing motion, the Alfvénic turbulence tends to move along the magnetic field direction. To find how turbulent eddies evolve in the direction parallel to the magnetic field, it is also necessary to consider the mixing motions associated with magnetic eddies and Alfvén waves with period equal to that of an eddy:

$$\frac{l}{v_l} \sim \frac{l_{||}}{v_{A}} \tag{1}$$

where  $l_{\parallel}$  is the parallel scale of the eddy and  $\nu_{\rm A}$  is the Alfvén velocity. The correlation between the parallel and perpendicular scales of sub-Alfvénic turbulence, i.e.,  $\nu_l \leqslant \nu_{\rm A}$ , eddies can be obtained as

$$l_{\rm II} \sim l^{\frac{2}{3}}.\tag{2}$$

This correlation shows that turbulent eddies are elongated along the direction of the magnetic field and it holds for eddies that are aligned with the local direction of the magnetic field that surrounds them. Incidentally, the concept of local magnetic field frame explains why, unlike the original GS95 treatment, the anisotropy of turbulence actually reflects the direction of

magnetic fields that percolate turbulent eddies. This result was confirmed by numerical simulations (Cho & Vishniac 2000; Maron & Goldreich 2001; Cho & Lazarian 2003). Due to this particular property of MHD turbulence, the velocities associated with a turbulent eddy are anisotropic so that the largest change in velocity is in the direction perpendicular to the local direction of the magnetic field. Thus, it is essential that the VGT is tracing the local magnetic field around eddies rather than the mean magnetic field.

It is worth mentioning that several approaches have been proposed to trace the magnetic field based on the MHD anisotropy relation (Equation (2)). The correlation function analysis (CFA) of the velocities and the principal component analysis for anisotropy (PCAA) were first proposed to study magnetic field morphology (Heyer et al. 2008), to estimate magnetization (Esquivel & Lazarian 2011; Esquivel et al. 2015), and to determine the contribution of the fast, slow, and Alfvén modes in observed turbulence (Kandel et al. 2016, 2017a, 2017b) using the theoretical understanding of MHD turbulence discussed above21. However, a numerical study by Yuen et al. (2018) showed that, compared with VGT, CFA and PCAA face several issues; in particular, the anisotropy may be distorted, eddies may be multi-centered, or the contours are not closed. These significantly degrade the determination of the direction of anisotropy, and thus the inferred magnetic field orientation through CFA and PCAA. Later Clark et al. (2014) proposed the rolling Hough transform (RHT) to study the magnetic field in the diffuse region based on the fact that socalled narrow "HI fibers" are aligned parallel to the magnetic field orientation. However, the RHT requires linear structures in the ISM (Clark et al. 2014).

Moreover, VGT as a superior technique has been successfully tested to trace the local magnetic field from both diffuse regions and absorbing media for the case of <sup>13</sup>CO emission with different abundances and densities (González-Casanova et al. 2019), while Hsieh et al. (2019) showed in numerical simulations that the VGT can map out the magnetic field structures of different physical depths in a molecular cloud using CO isotopologues with different optical depths and in the presence of weak self-gravity.

## 2.2. Molecules as Probes of Gas in Different Density Regimes

GMCs are the sites for most of the star formation occurring across the Milky Way and in other galaxies. The star formation regions are often observationally unresolved in GMCs. The gas in GMCs has an average number density of the order of  $10^2 \,\mathrm{cm}^{-3}$ and temperature of 10-30 K (Heyer et al. 2009), while the star formation clumps may have number densities around 10<sup>7</sup> cm<sup>-3</sup> and temperature as low as 10 K or even lower (Williams et al. 1994). Molecular tracers like <sup>12</sup>CO typically become optically thick, and therefore mostly trace the outer (low-density) regions of molecular clouds.  $^{13}$ CO, which is typically a factor of  $\sim$ 100 less abundant than <sup>12</sup>CO, and therefore usually optically thin, can be used to trace intermediate-density regions, as can the even less abundant isotopologue C<sup>18</sup>O. Transitions of the molecules CS, HNC, HCO+, and HCN have higher critical densities and are therefore used to trace intermediate- or high-density molecular gas. These molecules tend to either trace regions where the effect of self-gravitation is very strong, or gas that is just outside the selfgravitating regions. However, regions with high-density gas do not necessarily host star formation, that is, high density does not

 Table 1

 Observation Parameters for Seven Chemical Tracers Used in Our Analysis

Molecular Line	Line of Transitions	Frequency (GHz)	FWHM (arcsec)	$\xi$ (km s <sup>-1</sup> )	$\delta v ({\rm km~s^{-1}})$	Tracing Density	$\sigma_{T_R}$ (K)
<sup>12</sup> CO	J = 1-0	115.27	27.12	0.18	3.48	$\sim 10^2 \text{ cm}^{-3}$	0.113
<sup>13</sup> CO	J = 1-0	110.20	28.37	0.18	4.75	$\sim 10^3 \text{ cm}^{-3}$	0.053
C <sup>18</sup> O	J = 1-0	109.78	36.01	0.18	8.32	$\sim 10^4  \mathrm{cm}^{-3}$	0.053
CS	J = 1-0	48.99	63.82	0.21	9.61	$\sim 10^4 \text{ cm}^{-3}$	0.095
HNC	J = 1-0	90.66	34.48	0.22	4.97	$\sim 10^5 - 10^6 \text{ cm}^{-3}$	0.039
HCO <sup>+</sup>	J = 1-0	89.19	35.05	0.23	4.79	$\sim 10^5 - 10^6 \text{ cm}^{-3}$	0.018
HCN	J = 1-0	88.63	35.28	0.23	6.41	$\sim 10^5 - 10^6 \text{ cm}^{-3}$	0.019

**Note.** Note that for all molecules we have observed the ground state (J = 1 - 0) transitions.  $\xi$  is the velocity channel width of each molecular line cube. Note that the cubes are Nyquist sampled so the true velocity resolution is  $2\xi$ .  $\delta v$  is the velocity dispersion and  $\sigma_{T_R}$  is the per channel noise level of  $T_R$  for each data cube. Fissel et al. (2019) provides more details about the data reduction.

Type of Molecule, their Respective Transition Levels, Observing Frequency in GHz, Original Telescope Beam Full Width Half Maximum (FWHM) without Any Additional Smoothing in arcseconds, the Smallest Thickness of the Velocity Channel Slice, and the Approximate Molecular Hydrogen Density ( $N_{H_2}$ ) We Expect Each Molecule to Trace

necessarily indicate that the self-gravitation is strong enough to trigger gravitational collapse.

In summary, we expect that each molecular line will trace a different set of temperature, density, and excitation conditions. Therefore, using multiple molecular lines it is possible to study the cloud velocity and density structure in low-, intermediate-, and high-density molecular gas. Table 1 summarizes the properties of the molecular lines used in this study. Note that we only use the ground state (J=1-0) transition of each molecular line in our analysis.

### 3. Method

### 3.1. Velocity Gradient Technique

We use molecular line data from a survey with the 22 m Mopra telescope covering the Vela C GMC, covering 264°.62–266°.56 in Galactic longitude, and 0°.54–1°.92 in Galactic latitude. The observations are is described in detail in Fissel et al. (2019). The beam full width half maximum (FWHM) in arcminutes and the thickness of velocity slice in km s<sup>-1</sup> of different tracers are shown also in Table 1.

Vela C is a massive ( $M \sim 10^5 M_{\odot}$ ), relatively nearby GMC (*Gaia*-DR2 distance ~900 pc), which appears to be relatively young and unevolved (Yamaguchi et al. 1999; Netterfield et al. 2009; Hill et al. 2011). This molecular cloud is mostly cold ( $T_{\rm dust} < 15 \, {\rm K}$ ) and in early stages of star formation, though it has formed a 1 Myr cluster of stars which powers a compact H II region, RCW 36 (Ellerbroek et al. 2013). Since Vela C is dominated by a single velocity component in the range 0–12 km s<sup>-1</sup> (Fissel et al. 2019), it therefore provides a good opportunity for testing the VGT through the study of alignment between VCGs/VChGs and the magnetic field orientation inferred from polarization data. We infer the orientation of the projected magnetic field by rotating measurements of polarization angle made with BLASTPol at 500  $\mu$ m by 90° (Fissel et al. 2016).

Velocity centroid maps C(x, y) for all tracers are produced by integrating along the velocity axis of the position–position–

velocity (PPV) cube:

$$C(x, y) = \frac{\int dv T_R(x, y, v) \cdot v}{\int dv T_R(x, y, v)}$$
(3)

where  $T_R$  is the radiation temperature (in kelvin), and  $\nu$  is the line-of-sight velocity. For the analysis of observational data, the theory describing the statistics of fluctuations in the PPV cube is crucial (Lazarian & Pogosyan 2000). It predicts the anisotropy of the velocity channel maps (Lazarian et al. 2002).

Even when the velocity slice is thin, the channels can record more contribution from turbulent velocities (Lazarian & Pogosyan 2000; Yuen et al. 2019). Therefore, the gradients of thin VChGs are expected to trace the magnetic field orientation with high accuracy (Lazarian & Yuen 2018b). Thus, we also investigate the correspondence between VChGs and the magnetic field. To construct the velocity channel maps, we create integrated maps over a narrow velocity range  $\Delta \nu$  satisfying

$$\Delta v \leqslant \sqrt{\langle \delta v^2 \rangle} \tag{4}$$

where  $\delta v^2$  is the line-of-sight velocity dispersion. This is the criterion proposed in Lazarian & Pogosyan (2000) so that the velocity contribution in the velocity channel map dominates over the density contribution (see Table 1). Then the velocity channel map can be calculated also by integrating along the velocity axis:

$$Ch(x, y) = \int_{\nu_0 - \Delta\nu/2}^{\nu_0 + \Delta\nu/2} d\nu \ T_R(x, y, \nu)$$
 (5)

where  $v_0$  is the velocity corresponding to the central peak of the velocity profile along the line of sight. We follow the gradient calculation algorithm of velocity centroid maps from YL17, and velocity channel maps from Lazarian & Yuen (2018b), with the sub-block averaging method (YL17) applied. (Note that the sub-block averaging method is not just a smoothing method for suppressing noise in a region, but used to increase the reliability of the important statistical measure.) In this work, the sub-block size is selected as 24 pixels ( $\sim$ 1 pc, 12" per pixel for CO isotopologues, HCN, HNC, HCO<sup>+</sup>, and 24" per pixel for CS) which is enough for statistical accuracy. The polarization vector is averaged over the same sub-block size. In addition, Lazarian & Yuen (2018b) suggested a refinement of the velocity gradient

<sup>&</sup>lt;sup>5</sup> The data reduction and removal of the contribution to the polarized emission from dust in the diffuse ISM surrounding Vela C is described in Fissel et al. (2016). In our analysis, we use only data using the "intermediate" diffuse emission subtraction method from Fissel et al. The beam FWHM of the BLASTPol  $500\mu$ m polarization data is 2/5, which corresponds to  $\sim$ 0.6 pc at the distance to Vela C.

technique by using the moving window approach, which uses a continuous sub-block averaging, rather than dividing up the map into discrete sub-blocks. We apply the moving window to all our gradient maps unless specifically mentioned.

In practical observation, noise is present in spectroscopic data. Lazarian & Yuen (2018b) find that white noise would alter the alignment of gradients to the projected magnetic field. However, the alignment remains fairly good for data with an intensity signal to noise of 3 or greater, and only significantly diverges from the true gradient alignment angle when the signal to noise of the data approaches 1. Therefore, in the case of high noise, a Gaussian filter is proposed in Lazarian et al. (2017) to reduce the effect of noise in velocity centroid maps and velocity channel maps. In addition, in order to match the gradient after the sub-block averaging, the polarization data are first smoothed to the same angular resolution as molecular data. We average the polarization data over an area corresponding to the sub-block size in order to match the resolution of the gradient maps. With a sub-block size 24 pixels, the effective resolution of both gradients and polarization is 4/8 (9.6 for CS) which is larger than the minimum resolution of polarization 2.5. Note that neither the polarization nor the spectroscopic data are filtering out scales smaller than 4.8 (9.6 for CS), and there could be small-scale magnetic field structures that cannot be resolved with our sub-block averaging method.

## 3.2. Alignment Measure

The orientation of gradients from VGT is compared with the magnetic filed inferred from BLASTPol polarization. The relative orientations between the  $90^{\circ}$  rotated gradients and project magnetic field directions from polarization angles are measured by the alignment measure (AM) used:

$$AM = 2\left(\langle \cos^2 \theta_r \rangle - \frac{1}{2}\right) \tag{6}$$

where  $\theta_r$  is the angular difference between the gradient vector rotated by 90° and the magnetic field vector derived from polarization in a single sub-block;  $\langle ... \rangle$  indicates the average over all sub-blocks.

The range of AM is [-1, 1]. There are three important cases for the value of AM:

- 1. AM = -1: in this case the gradients are perpendicular to the projected magnetic field;
- 2. AM = 0: the gradients are neither perpendicular nor parallel to the magnetic field;
- 3. AM = 1: the gradients are parallel to the projected magnetic field, which implies a perfect alignment.

AM is a parameter used to quantify the relative orientation between two vectors. Note that since AM is insensitive to the sign of the velocity gradient, e.g.  $AM(\theta) = AM(-\theta)$ , it is advantageous to test the performance of the VGT in terms of the orientation of plane-of-the-sky magnetic fields, i.e., the larger the AM, the better alignment between the measurements from VGT and polarization.

# 4. Tracing the Magnetic Field Using VGT over a Larger Range of Densities

4.1. Low-density Tracers: 12CO, 13CO, and C18O

<sup>12</sup>CO, <sup>13</sup>CO, and C<sup>18</sup>O typically trace gas with H<sub>2</sub> number density between 10<sup>2</sup> and 10<sup>4</sup> cm<sup>-3</sup>, which is the typical density

for a young self-gravitating molecular cloud (Crutcher 2012). Because their lines tend to have lower optical depths, <sup>13</sup>CO and C<sup>18</sup>O can trace molecular gas over a larger range of densities, while optically thick <sup>12</sup>CO traces the lower-density outer cloud regions. In YL17, we see that, by combining the gradient vectors and polarization measurements from the same region, we can determine whether a region is optically thick or thin, and whether the self-gravity is dominant in a particular region or not.

Figure 1 shows the normalized distribution of the relative orientation between rotated VCGs/VChGs and the inferred magnetic field from polarization using <sup>12</sup>CO, <sup>13</sup>CO, and C<sup>18</sup>O as tracers. The distribution is constructed by calculating gradients for each map pixel, without using sub-block averaging. We find that the set of rotated gradient alignment angles is roughly consistent with a Gaussian distribution. The expectation values of VCGs are located near 13°.5, while for VChGs the expectation values are decreasing with increasing critical density of each tracer. Considering the systematic uncertainty in polarization data is less than 10° (see the Appendix), the results support our theoretical consideration that the velocity gradient rotated by 90° tends to align with the magnetic field.

Figure 2 shows the orientation of VCGs, VChGs, and the magnetic field obtained from polarization with sub-block averaging applied. Figure 2 also shows that using C<sup>18</sup>O VChGs reflects the central structure of the cloud, while <sup>12</sup>CO and <sup>13</sup>CO determine the structure of the outskirts. Considering the systematic uncertainty in polarization data is approximately 2°.07 (see the Appendix), these three tracers show similar agreement with the magnetic field inferred from polarization data based on the estimation of AM.

### 4.2. High-density Tracers: HCN, HNC, HCO<sup>+</sup>, and CS

Molecular CS is well known for tracing dense clumps in the molecular clouds in the Milky Way. Also, recent multi-line surveys of nearby spiral galaxies (Bayet et al. 2009) of this molecule in extragalactic environments have revealed low J ( $J \le 4$ ) transitions of CS trace gas densities of the order  $10^5 \, \mathrm{cm}^{-3}$ , even close to  $10^6 \, \mathrm{cm}^{-3}$ . Estimates of the effective excitation density of CS from Shirley (2015) show that cold CS J = 1 - 0 typically traces densities of  $\sim 10^4 \, \mathrm{cm}^{-3}$ .

HCN and HNC are two species that have routinely been used as tracers of star formation regions in molecular clouds (Turner et al. 1997). In fact, HCN is used to trace the same approximate densities as the low-J CS molecule, and hence the gas that it traces is not necessarily in a self-gravitating star formation region. HNC has a similar critical density to that of HCN. Therefore, HNC and HCN should be good tracers for higher-density star formation gas which might be self-gravitating. Pety et al. (2017) showed that HNC is a better molecular tracer than HCN when probing low-J lines, based on the analysis of visual extinction and line-integrated intensities. We note that the HCN J=1-0 has a hyperfine structure which complicates the interpretation of the VCGs. Also the HCN emission has a lower integrated line emission compared to HNC (Fissel et al. 2019).

Compared to the other three tracers, HCO<sup>+</sup> is more often used as a tracer of ionized gas (e.g., see Cleeves et al. 2015). However, 80% of the HCO<sup>+</sup> and HCN emission originates in non-self-gravitating regions of molecular clouds (Vollmer et al. 2017). HCN and HCO<sup>+</sup> emission lines can therefore both be used to trace the dense gas around self-gravitating regions.

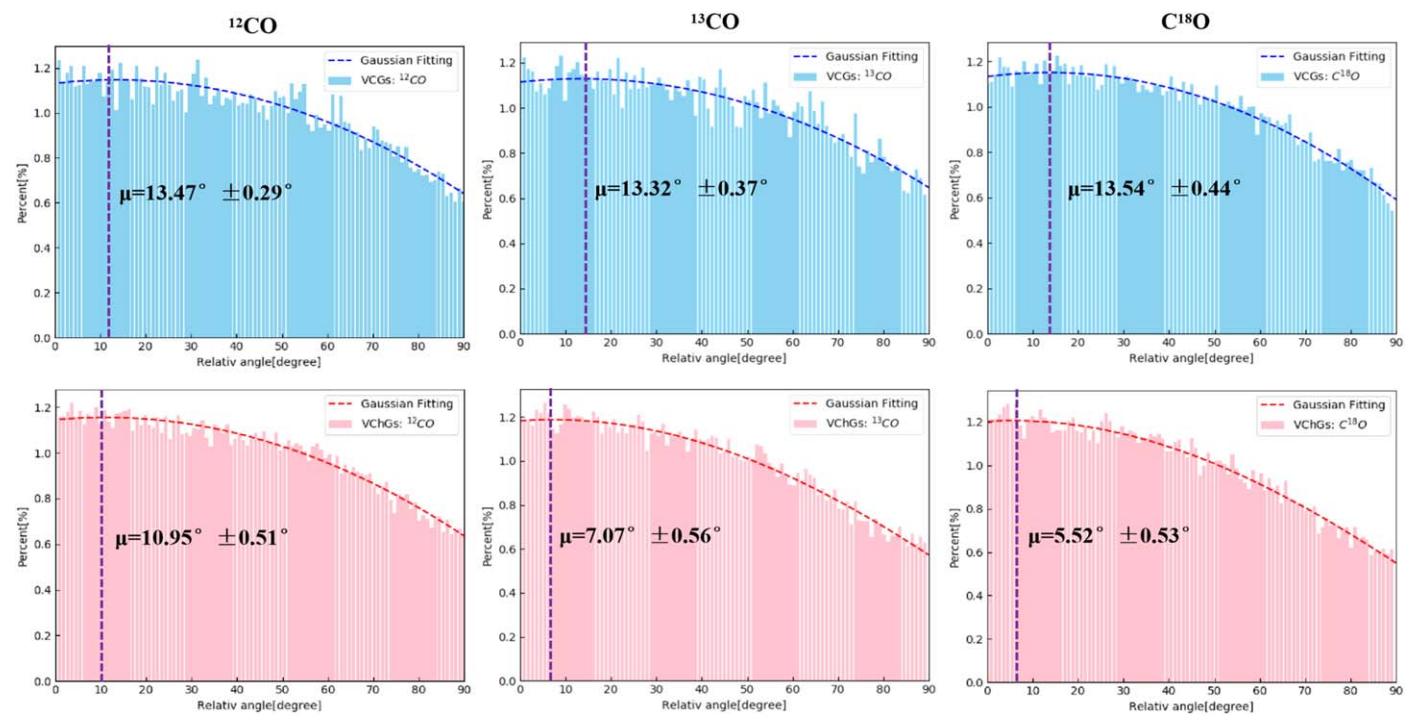


**Figure 1.** Normalized distributions of alignments between rotated velocity centroid gradients (VCGs, top row)/velocity channel gradients (VChGs, bottom row), and magnetic field inferred from polarization. The distribution is drawn using raw gradients of each pixel without sub-block averaging. The dashed line is a Gaussian fit to the distribution, where  $\mu$  is the expectation of the distribution. The vertical axis is the relative probability of the relative angle. The uncertainty is given by the standard error of the mean, i.e., the standard deviation divided by the square root of the sample size, while the systematic uncertainty in polarization data is given in the Appendix.

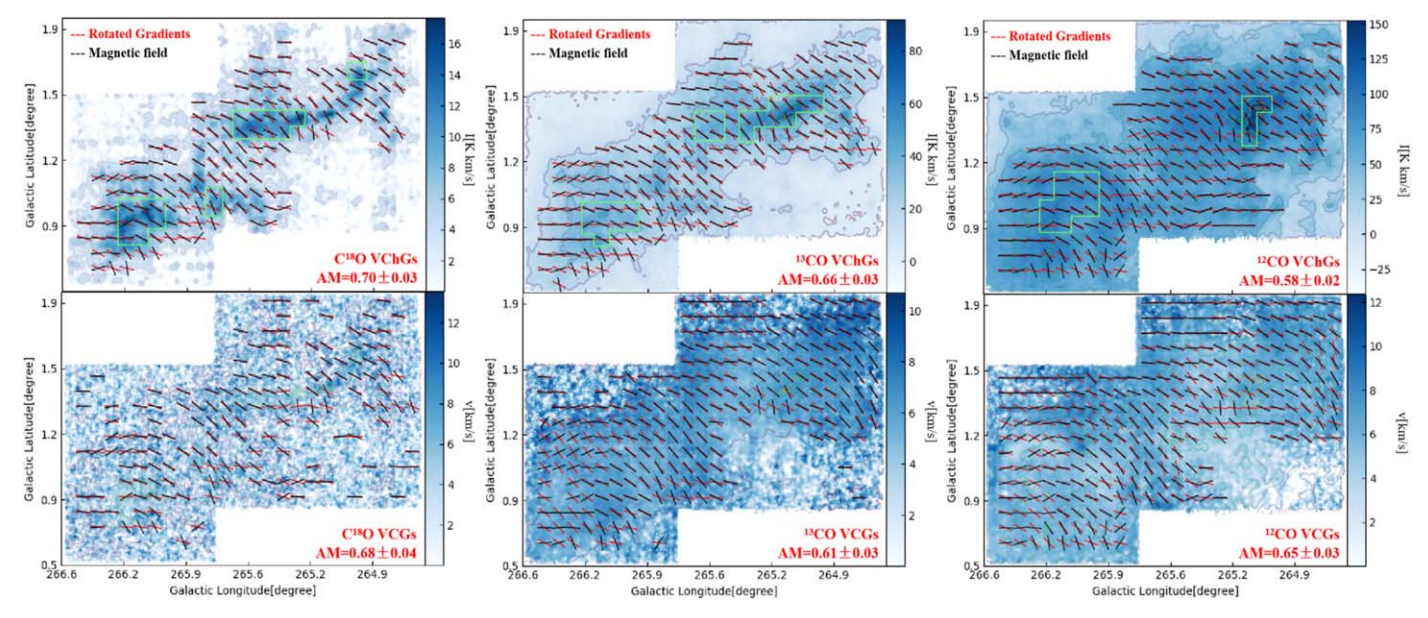


**Figure 2.** Orientation of VChGs (top row), VCGs (bottom row), and the magnetic field obtained from polarization (black line segment). The VCGs and VChGs are rotated by 90°. The left panels use C<sup>18</sup>O as a tracer, the middle panels show <sup>13</sup>CO, and the right panels show <sup>12</sup>CO. The background images are moment zero maps (integrated line intensities) for VChGs, and first moment maps for VCGs. Green contours in the top panels indicate the high-intensity regions in which all pixels are above the 95th percentile in integrated line intensity. (See Fissel et al. 2019 for details of each data set.)

Figure 3 shows the normalized distribution of the relative orientation between rotated VCGs/VChGs and the inferred magnetic field from polarization, using CS, HCN, HNC, and HCO<sup>+</sup>. We do not apply sub-block averaging when constructing the distributions, but use the raw gradients for each pixel. We find that the distribution is consistent with a Gaussian distribution. However, the expectation values of VChGs are

 $\sim$ 5°.5, lower than the expectation values for the  $^{12}$ CO, and  $^{18}$ O lines. CS and HNC show smaller expectation values of VCGs compared to HCN and HCO $^+$ .

Figures 4 and 5 show the orientation of VCGs and VChGs using HCN, HNC, HCO<sup>+</sup>, and CS, and the magnetic field obtained from polarization with sub-block averaging applied. Figure 5 shows that CS is able to detect a clear structure of

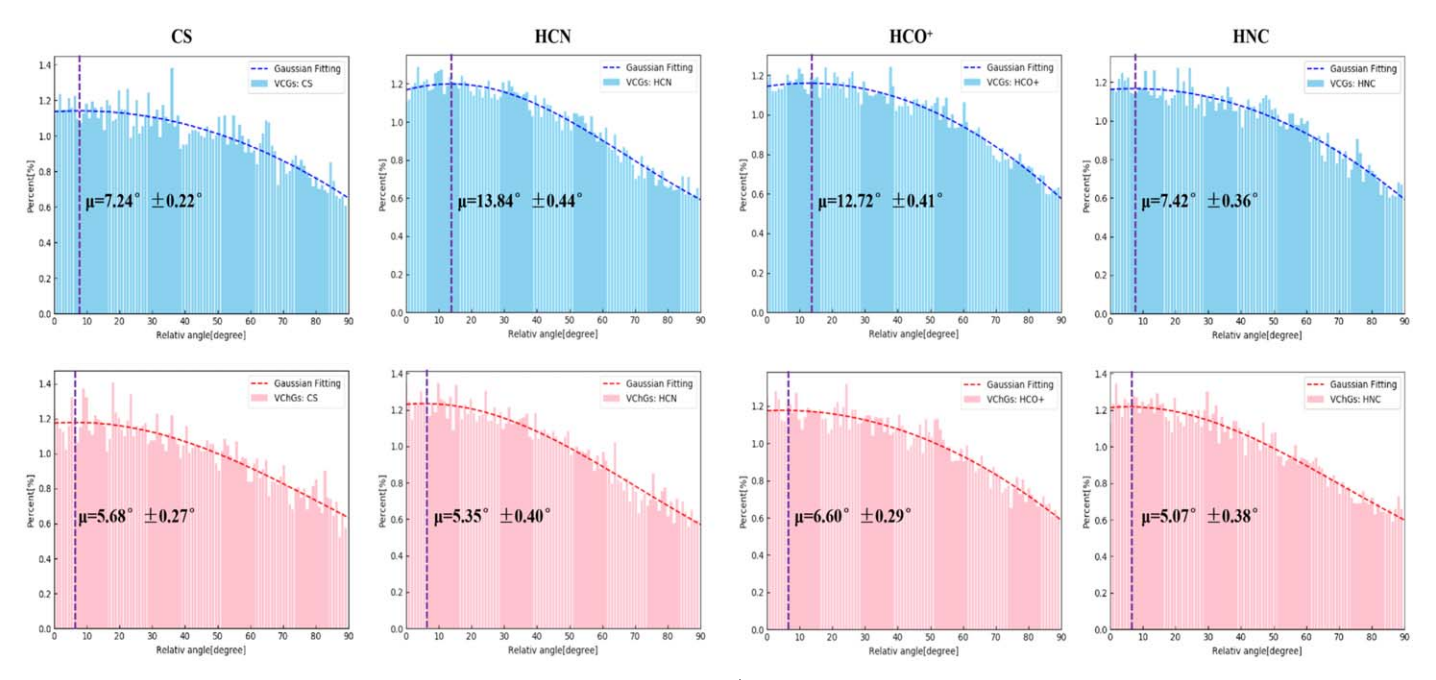
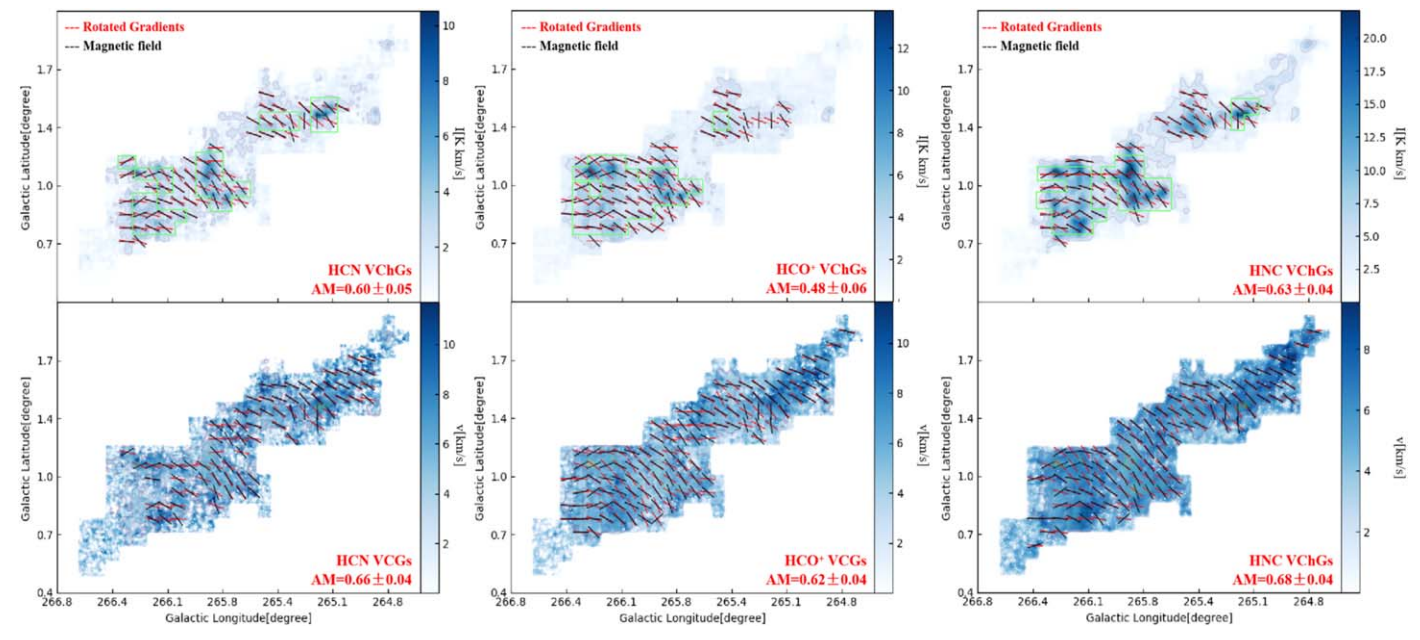


Figure 3. Normalized distribution of alignment between rotated VCGs (top row)/VChGs (bottom row), and the magnetic field inferred from polarization. The distribution is drawn by using raw gradients of each pixel, without sub-block averaging. The dashed line is a Gaussian fit to the distribution, where  $\mu$  is the expectation of the distribution. The vertical axis is the relative probability of the relative angle. The uncertainty is given by the standard error of the mean, i.e., the standard deviation divided by the square root of the sample size, while while the systematic uncertainty in polarization data is given in the Appendix.



**Figure 4.** Orientation of VChGs (top row), VCGs (bottom row), and the magnetic field (black line segment) obtained from polarization. The VCGs and VChGs are rotated by 90°. The left column represents HCN as the tracer, the second column is HCO<sup>+</sup>, and the third is HNC. Green contours in the top panels indicate the high-intensity regions in which all pixels are above the 95th percentile in integrated line intensity. (See Fissel et al. 2019 for details of each data set.)

Vela C using VChGs, and shows perhaps the best agreement with the polarization inferred magnetic field orientation, with AM=0.70. Among the four tracers, HNC and CS appear to best trace the magnetic field.

# 4.3. Contribution from the Foreground and Background

In a low Galactic latitude cloud, such as Vela C, foreground and background material can change the observed cloud

magnetic field orientation. In contrast, the VGT method for tracing magnetic fields is only sensitive to the molecule probed, and molecular line cubes can be studied solely over the velocity range associated with the molecular cloud of interest. Using the VGT it should therefore also be possible to trace the magnetic field in different layers of the cloud, by targeting lines that trace different ranges of density. Thus, the VGT using molecular tracers provides information on the localized magnetic field corresponding to species in the cloud, while polarization

Table 2 Expectation value  $\mu$  of the Relative Angle between Rotated VCGs/VChGs and the Magnetic Field Inferred from Polarization, without Sub-block Averaging

Molecule Line	μ (VCGs)	μ (VChGs)	AM (VCGs)	AM (VChGs)
<sup>12</sup> CO	$13^{\circ}\!.47 \pm 0^{\circ}\!.29$	10°95 ± 0°51	$0.65 \pm 0.03$	$0.58 \pm 0.02$
<sup>13</sup> CO	$13^{\circ}.32 \pm 0^{\circ}.37$	$7.07 \pm 0.56$	$0.61 \pm 0.03$	$0.66 \pm 0.03$
$C^{18}O$	$13.64 \pm 0.37$	$5^{\circ}.52 \pm 0^{\circ}.53$	$0.68 \pm 0.04$	$0.70 \pm 0.03$
CS	$7^{\circ}.24 \pm 0^{\circ}.22$	$5.68 \pm 0.27$	$0.63 \pm 0.02$	$0.70 \pm 0.02$
HCN	$13.84 \pm 0.44$	$5^{\circ}.35 \pm 0^{\circ}.40$	$0.66 \pm 0.04$	$0.60 \pm 0.05$
HNC	$7.42 \pm 0.36$	$5^{\circ}.07 \pm 0^{\circ}.38$	$0.63 \pm 0.04$	$0.68 \pm 0.04$
HCO <sup>+</sup>	$12^{\circ}.72 \pm 0^{\circ}.41$	$6.60 \pm 0.29$	$0.48\pm0.06$	$0.62 \pm 0.04$

**Note.** The uncertainty is given by the standard error of the mean, i.e., the standard deviation divided by the square root of the sample size, while the systematic uncertainty in polarization data is given in the Appendix.

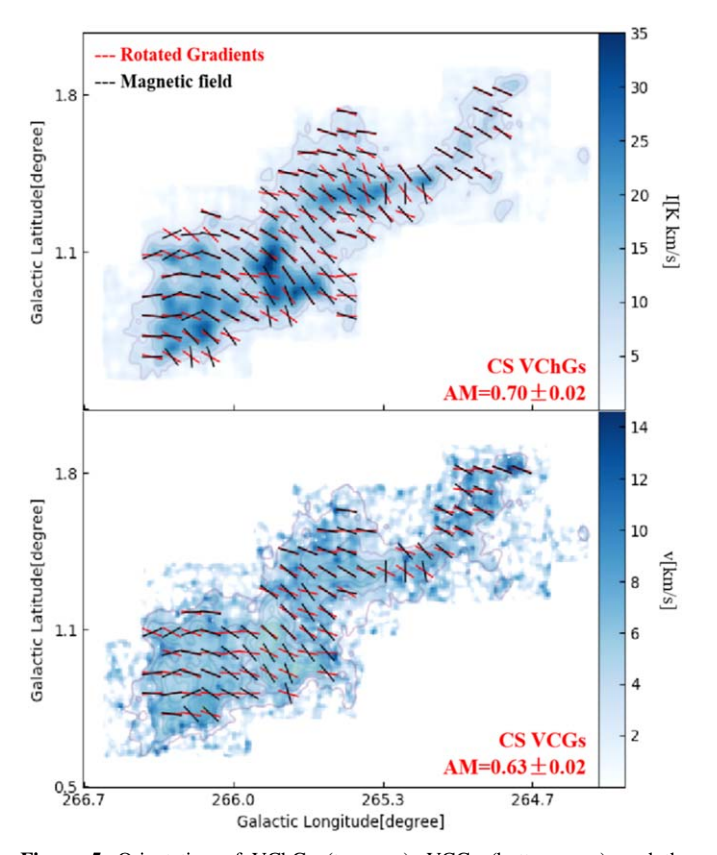


**Figure 5.** Orientation of VChGs (top row), VCGs (bottom row), and the magnetic field (black line segment) obtained from polarization. The VCGs and VChGs are rotated by  $90^{\circ}$ .

accumulates information along the line of sight, i.e., the VGT and polarization are tracing different components of the magnetic field. If we want to fairly compare the VGT and polarization, we should consider the contribution from the foreground and background.<sup>6</sup>

Fissel et al. (2016) attempted to remove the contribution of the foreground and background dust to the BLASTPol 500  $\mu$ m polarization data by using two different methods to model the diffuse polarized dust emission, and subtracting their model from the data. However the systematic uncertainty associated with removing the diffuse polarized emission is expected to most affect polarization angles toward regions of low column density within Vela C. We note that several locations where the BLASTPol inferred magnetic field direction differs from the velocity gradient inferred field direction are toward the edge of the map in low column density regions of Vela C.

Table 2 shows the expectation value  $\mu$  of the relative angle between the rotated gradients of each molecular tracer and the magnetic field inferred from dust polarization. From Table 2, we find that low-density tracers, i.e.,  $^{12}\text{CO}$  and  $^{13}\text{CO}$ , indeed show larger deviation between the rotated VChGs and magnetic fields inferred from the polarization than high-density tracers. As mentioned above, for low column density regions we expect a larger systematic uncertainty in the polarization angle associated with background/foreground polarized emission subtraction, so it is not surprising that  $^{12}\text{CO}$  and  $^{13}\text{CO}$ , which show emission across the entire mapped area, show a larger deviation from the VChG and VCG inferred magnetic field orientation.

In addition, we find that VChGs show approximately  $\mu \sim 6^{\circ}$ offsets for dense tracers, which are smaller than those of VCGs. Noise is one possible factor contributing to the larger deviations of the VCGs compared to VChGs; for example, the map of VCGs is integrating over the whole velocity range of the PPV cube, while for VChGs the map is integrating over a narrow velocity range  $\Delta v$ . There is also a second possibility for the worse alignment measures for the VCG maps. Although Vela C is dominated by a single velocity component, there are multiple velocity components in some parts of Vela C (see Figure 1 in Fissel et al. 2019). The VCG analysis implicitly assumes only one velocity component. We note also that the HCN J = 1 - 0 line has a hyperfine structure, which makes calculating line velocity centroids more difficult. In addition, RCW 36 is a compact H II region on Vela C. However, the H II region is compact ( $\sim$ 1 pc in size) and as such only comprises a small portion of the map (Fissel et al. 2016). The contribution from RCW 36 is therefore slim.

# 5. Tracing the Magnetic Field from the Low-density to High-density Gas Regions

# 5.1. Low-density Gas Regions

Figure 2 shows that the integrated velocity channel maps, i.e. the moment = 0 maps, are able to trace the cloud's column density structure. VChGs of  $^{12}$ CO and  $^{13}$ CO appear to mostly

<sup>&</sup>lt;sup>6</sup> Note that Fissel et al. (2019) shows that Vela C is dominated by a single velocity component in the range 0–12 km s<sup>-1</sup>, while there might be multiple velocity components in a wider velocity range. For a fair comparison with polarization, we did not constraint the PPV cube to a particular velocity range, but kept its original velocity range −20–30 km s<sup>-1</sup> for the presented results. We repeat our VCG and VChG analyses but limit the velocity range to 0–12 km s<sup>-1</sup>. The AM (with error bar  $\sim$ ±0.03) is generally 0.05 lower than the presented results. AM values for single/multiple-component analyses still give similar values. We therefore expect the bulk of the signal in both data sets can be reasonably well compared and is dominated by signals from Vela C, although both polarization and spectroscopic data are not entirely constrained to Vela C.

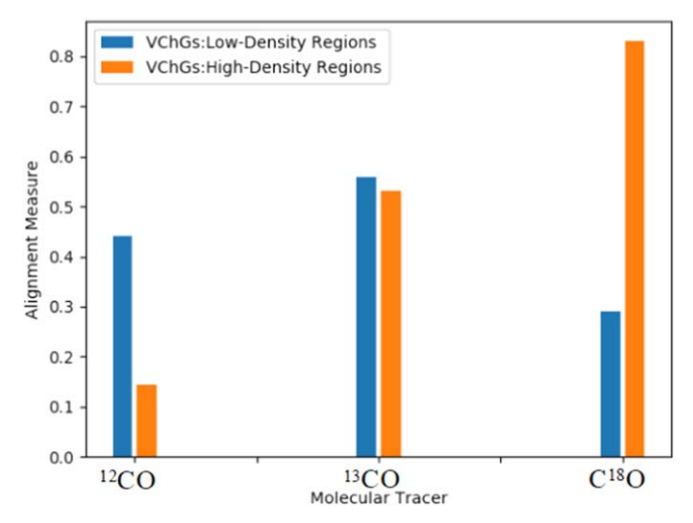


**Figure 6.** Alignment measure of low-intensity and high-intensity regions as traced by moment = 0 maps (shown in Figure 2), using VChGs for molecular tracers  $^{12}$ CO,  $^{13}$ CO, and  $C^{18}$ O.

trace the low- to intermediate-density material of the cloud, as they become optically thick toward high column density cloud sightlines.

Due to the lower optical depth of C<sup>18</sup>O, its emission lines trace deeper into the cloud, and therefore include cloud structures over a larger range of densities. In this case, we can use <sup>12</sup>CO, <sup>13</sup>CO to get a fairly good idea of the magnetic field structure in the outer layers of the cloud and use C<sup>18</sup>O to better trace higher-density structure.

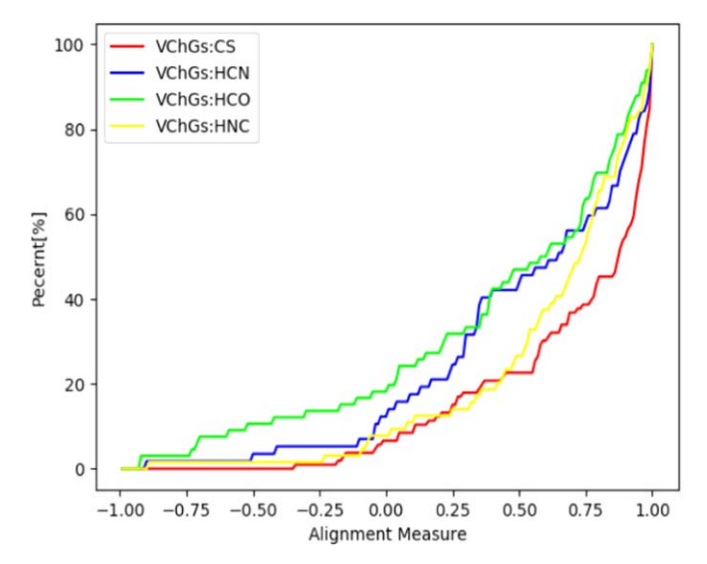
We therefore propose a method that uses multiple molecular lines as a combined tracer for magnetic field in GMCs, even if parts of the cloud are strongly self-gravitating. We separate each moment = 0 map of the Vela C cloud into low-intensity and high-intensity regions. The high-intensity region is defined by the percentile of the integrated line intensity: we take as the high-intensity region all pixels that are above the 95th percentile in integrated line intensity, while our definition of low-intensity gas is all the pixels that are below this threshold.

Figure 6 compares the alignment measure for the low-intensity and high-intensity regions (high-intensity regions for each tracer are indicated with green contours in Figures 2, 4, and 5), traced by <sup>12</sup>CO, <sup>13</sup>CO, and C<sup>18</sup>O. We find that for VChGs, <sup>12</sup>CO shows little alignment toward the high-intensity regions while C<sup>18</sup>O shows better alignment in high-intensity than in low-intensity regions. The weak integrated line intensities of C<sup>18</sup>O toward low column density cloud regions likely contributes to the lower AM values observed toward low column density sight lines.

## 5.2. High-density Gas Regions

As is described above, the CS, HNC, HCN, and HCO<sup>+</sup> are used as dense gas tracers. Although HCN and HCO<sup>+</sup> are usually generated in non-self-gravitating regions, they can be used to trace gas that is near the self-gravitating regions. Lower-density tracers <sup>12</sup>CO <sup>13</sup>CO and the intermediate-density tracer C<sup>18</sup>O can also be applied to relatively diffuse regions that are near the strong self-gravitating molecular core.

From Figures 5 and 4, it is obvious that both CS and HNC show excellent alignment between gradients and the magnetic field. Figure 7 shows the cumulative plot of the AM, when using VChGs to trace the magnetic field by CS, HCN, HCO+, and



**Figure 7.** Cumulative plot of alignment measure, with respect to different molecular tracers: CS, HCN, HCO<sup>+</sup>, and HNC. VChGs are used here.

HNC. CS and HNC show a very strong increase in the cumulative fraction over the AM range [0.5, 1.0].

HNC and CS give a more robust performance than the others. We therefore propose to use HNC or CS to trace the magnetic field in the dense gas regions (i.e.,  $H_2$  density  $\sim 10^4 - 10^6 \, \text{cm}^{-3}$ ) of GMCs.

Furthermore, we propose including HNC in the inferred magnetic field orientation map made from a combination of multiple molecular line tracers. <sup>12</sup>CO, <sup>13</sup>CO, and C<sup>18</sup>O provide the structure of the magnetic field toward low and intermediate column density gas. Taking into account the dense region traced by HNC which traces higher densities on average than CS, we can therefore infer the plane-of-sky component of the magnetic field orientation over a wide range of cloud densities in GMCs.

Figure 8 shows the magnetic field structure of Vela C obtained from VChGs using a combination of the multi-tracers <sup>12</sup>CO, <sup>13</sup>CO, C<sup>18</sup>O and HNC. The map is produced as follows: using velocity channel maps, we compare the structure contours<sup>7</sup> as discussed above from different molecular tracers and remove the gradients calculated from the tracer with lower critical density in the overlap region but keep the gradients calculated from the tracer with higher critical density. The combination of multiple tracers shows a better alignment measure overall than any single molecular line tracer.

### 5.3. Re-rotation Test

In extremely high-density cloud regions, self-gravity can be the main force affecting the dynamics of the gas in GMCs. We expect the gradients to be aligned parallel to the magnetic field in the presence of gravitational collapse, i.e., the direction of the gradient should flip 90° (Yuen & Lazarian 2017b). In this section we search for the signature of gravitational collapse in Vela C using VCGs and VChGs.

We explore this by re-rotating the gradients by 90° again at the high-intensity cloud regions. This is equivalent to rotating the

 $<sup>^7</sup>$  The structure contour is a curve connecting points having the same particular value. We use the structure contour to highlight the main structure of Vela C for each tracer, as shown in Figure 2. The value selected for  $^{12}\text{CO}$  is  $50~\text{K km s}^{-1}$  and above,  $15~\text{K km s}^{-1}$  for  $^{13}\text{CO}$ ,  $3~\text{K km s}^{-1}$  for  $^{18}\text{O}$ ,  $5~\text{K km s}^{-1}$  for Cl $^{18}\text{O}$ ,  $5~\text{K km s}^{-1}$  for CS,  $4~\text{K km s}^{-1}$  for HNC, and  $2~\text{K km s}^{-1}$  for HCN and HCO $^+$ .

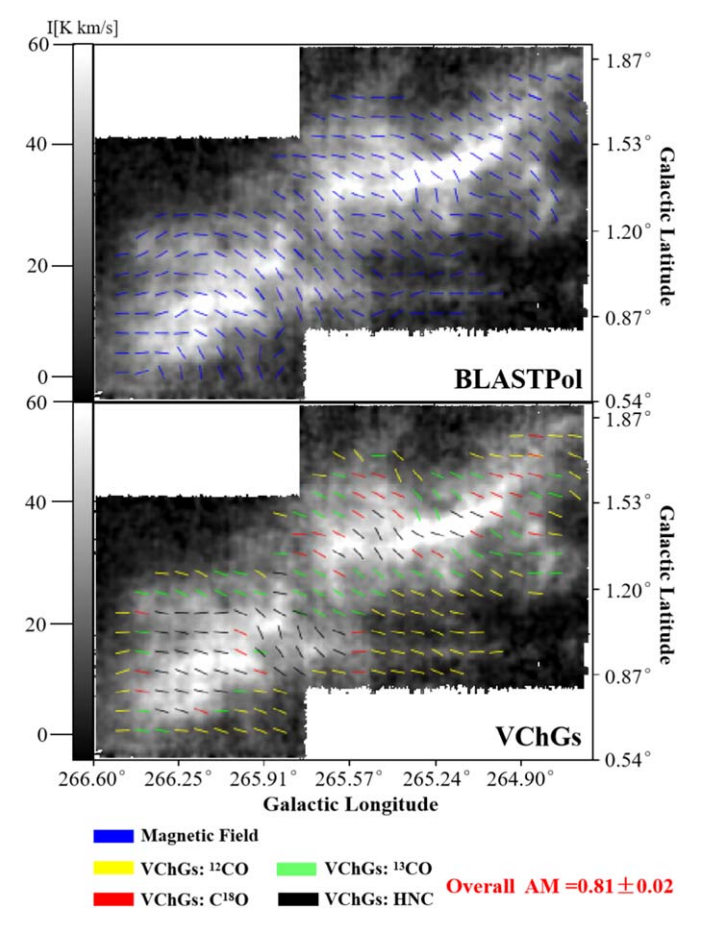


**Figure 8.** Top: orientation of magnetic field inferred from BLASTPol 500  $\mu$ m polarization data. Bottom: planar orientation of the magnetic field obtained by rotated VChGs using molecular tracers <sup>12</sup>CO (yellow line segment), <sup>13</sup>CO (lime line segment), C<sup>18</sup>O (red line segment), and HNC (black line segment). The background intensity map is traced by <sup>13</sup>CO.

gradients by  $90^{\circ}$  not toward high-intensity regions, but only low-intensity regions. For  $^{12}$ CO,  $^{13}$ CO, and  $^{18}$ O, we vary the threshold for the definition of high-intensity region from the 75th percentile in integrated line intensity, for which AM is close to 0, to the 100th percentile which means that there is no re-rotation. For CS, HCN, HNC, and HCO $^{+}$ , we change the range of high-intensity region from the 90th percentile, since with the threshold at the 90th percentile the AM is already close to 0.

Figure 9 shows the AM variation with different moment =0 map percentile thresholds defining the re-rotated region. It shows that the peak value of AM among all tracers is achieved at 100th percentile which means no re-rotation is required for both VCGs and VChGs to get good alignment with polarization. Thus the high-intensity region contributes positively to the whole AM value, among all tracers. Therefore we conclude that strongly self-gravitating, collapsing regions constitute only a small fraction of the cloud area within Vela C. This, however, does not prevent molecular gas in small-scale regions below the resolution limit of the Mopra data from collapsing and forming stars (Hu et al. 2019a).

#### 6. Discussion

# 6.1. Extracting Magnetic Field Orientation for Gas in Different Density Regimes

Molecular tracer maps with different optical depth provide spectroscopic information on gas dynamics up to a certain line-of-sight depth. The concept of gradient tomography was first discussed in Lazarian & Yuen (2018a) by considering the effective accumulation line-of-sight depth of synchrotron polarization data at different wavelengths. Both the synchrotron polarization data in the presence of strong Faraday rotation and the gas spectroscopic data in the presence of optically thick radiative transfer share the same concept that the contribution of gas dynamics with line-of-sight depth larger than some certain physical boundary would be effectively noise. Lazarian & Yuen (2018a) showed that, by stacking the gradient maps from the polarized synchrotron intensities measured from different frequencies, one can create 3D tomography information on the magnetic field. The number of layers in the gradient tomography completely depends on how many individual frequency measurements one has taken for the synchrotron data. Hsieh et al. (2019) implemented an analogous idea in the case of multiple molecular tracer maps using the SPARX radiative transfer code. For our analysis of the Vela C data each molecular tracer samples a different range of densities. Assuming the excitation temperature of Vela C is approximately 10 K and cosmic microwave background brightness temperature 2.725 K, Fissel et al. (2019) then calculated that the optical depth  $\tau_{18}$  for C<sup>18</sup>O typically ranges from 0.015 to 0.18, with a median value of 0.026. Assuming a [<sup>13</sup>CO/C<sup>18</sup>O] ratio of 10 and a [ $^{12}$ CO/ C $^{18}$ O] ratio of 400, this implies a typical  $\tau_{12} = [^{12}$ CO/ C $^{18}$ O] $\tau_{18}$  in the range of 6 to 72, and  $\tau_{13}$ in the range of 0.15-1.8. We can therefore expect that the velocity gradients tell us about the plane-of-sky component of the magnetic field over different density ranges, as shown Figure 10.

If the velocity gradient can be used to determine the magnetic field orientation over different cloud density regimes, this also has implications for the efficiency of dust grain alignment as a function of density. Dust grains in molecular clouds are thought to be aligned by radiative alignment torques (RATs; see Lazarian & Hoang 2007), and in deeply embedded cloud regions the alignment efficiency may be lower as the photons of the interstellar radiation field with wavelength comparable to the grain size would be selectively extinguished. However, some observational studies and numerical simulation indicate that grains can be effectively aligned for moderately extinguished dust sightlines (Bethell et al. 2007; Alves et al. 2014; Fissel et al. 2016). Moreover, the radiation of the embedded stars can play an important role for the RAT alignment (Whittet et al. 2008). The fact that the BLASTPolinferred magnetic field orientation shows a higher degree of alignment with the VGT of intermediate- or high-density tracers toward high column density sightlines would seem to indicate that dust grains are efficiently aligned in molecular gas with number density  $\approx 10^4$  cm<sup>-3</sup> or greater, and therefore that dust polarization can trace the magnetic field of intermediateand high-density gas. While from numerical simulations it has been confirmed that dust grains remain well aligned even at high densities  $n \ge 10^3$  (Seifried et al. 2019), this issue requires further studies with higher-resolution molecular line observations and polarization data.

# 6.2. Applicability of the VGT to Other Molecular Clouds

The gradient technique, which shows very good alignment with the magnetic field orientation obtained from polarization data, is a promising method to infer the magnetic field morphology over a wide range of physical conditions. Low-resolution polarization

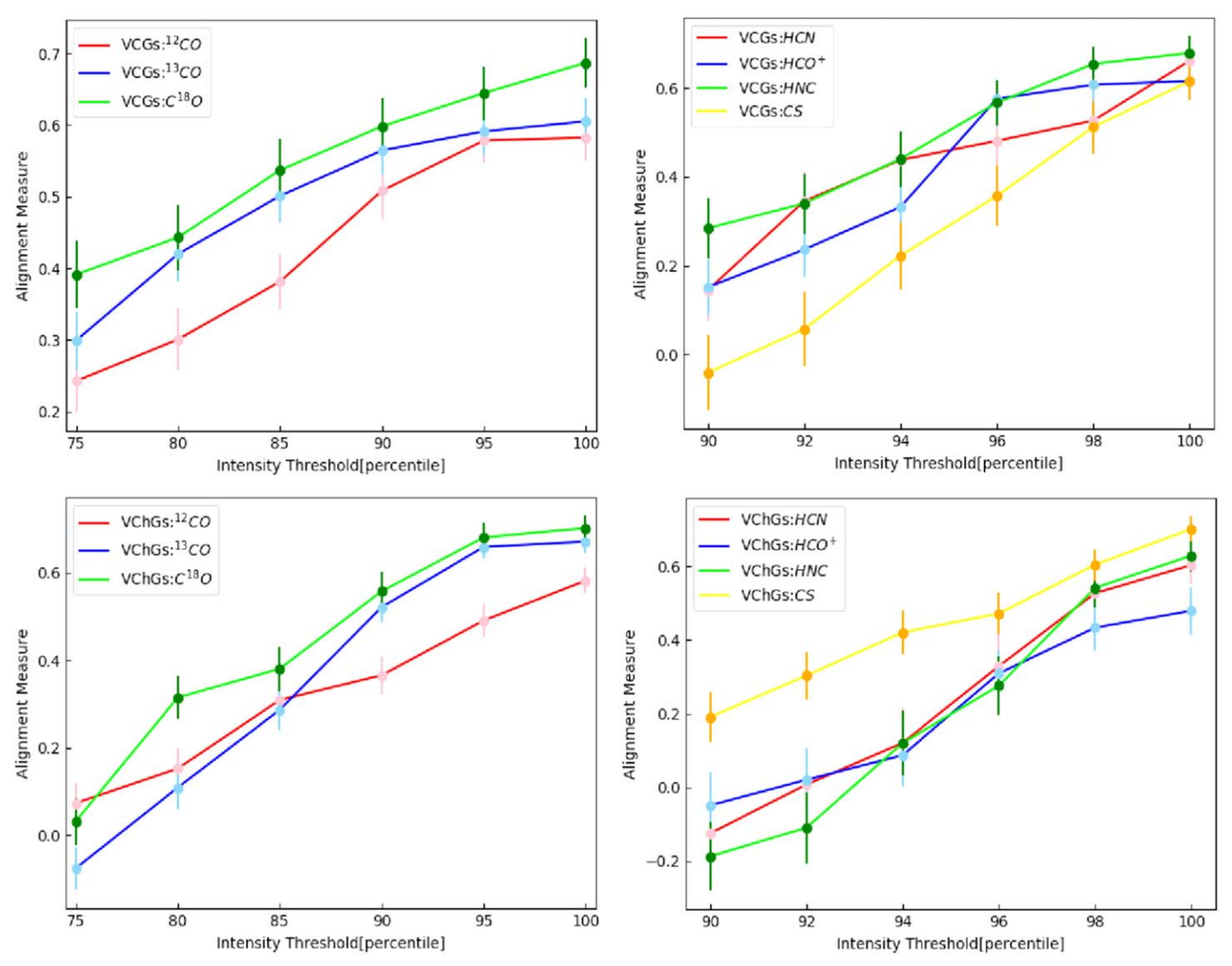


**Figure 9.** Variation of alignment measure calculated over the whole molecular line map with different re-rotated threshold. The horizontal axis is the threshold for re-rotation. When the density exceeds the threshold, we re-rotate the gradients in that region. The left column is testing with <sup>12</sup>CO, <sup>13</sup>CO, and C<sup>18</sup>O. The right column is for CS, HCN, HNC, and HCO<sup>+</sup>. The error bar is given by the standard error of the mean, i.e., the standard deviation divided by the square root of the sample size.

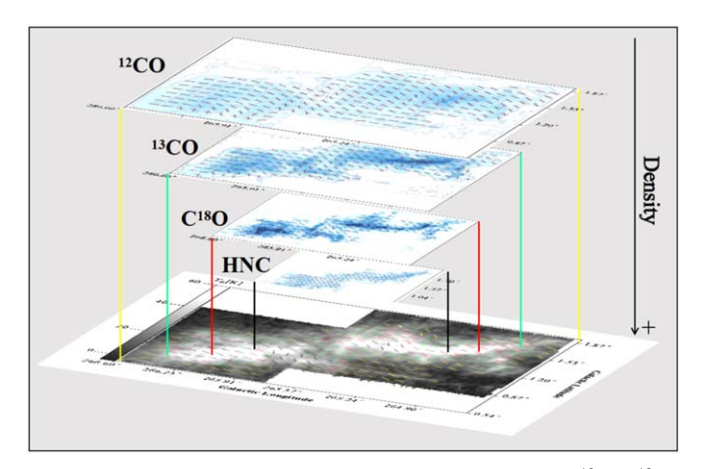
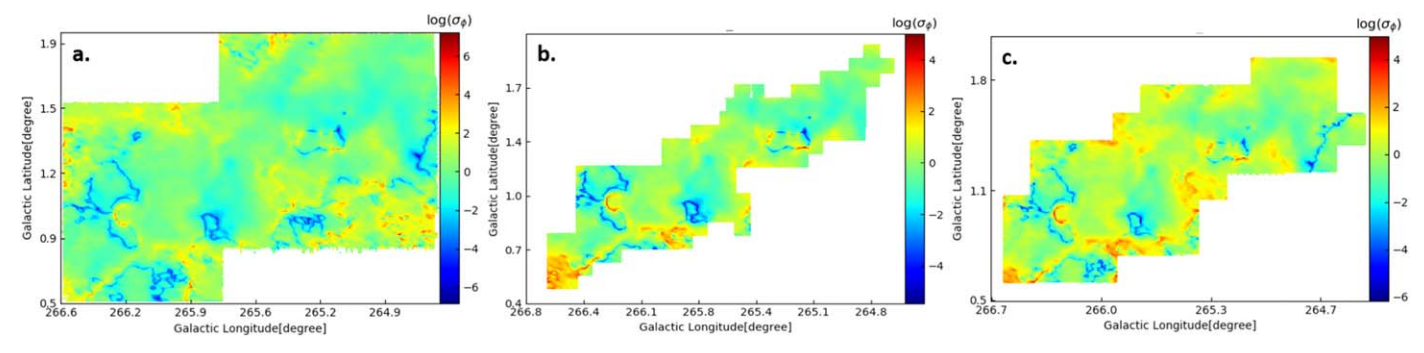


Figure 10. Cartoon of gradient tomography maps stacking from  $^{12}\mathrm{CO}, \, ^{13}\mathrm{CO}, \, \mathrm{C}^{18}\mathrm{O},$  and HNC.

data are now universally available from Planck all-sky data, while higher-resolution polarimetry data have been obtained from stratospheric and ground-based instruments. However, dust polarization may not be sensitive to the magnetic field within deeply embedded high-density regions, where the efficiency of grain alignment due to radiative torques is expected to be less efficient (Lazarian & Hoang 2007). In addition, it is very difficult to determine the magnetic field structure from polarization data when there are multiple dust clouds along the line of sight. However, the gradient technique can make use of readily available large-scale molecular line surveys, such as CHAMP (Stolle et al. 2006) and ThRuMMs (Nguyen et al. 2015), or the neutral hydrogen atom distribution survey (Hi4PI Collaboration et al. 2016) and the COMPLETE survey (Ridge et al. 2006), to provide measurements of the magnetic field orientations, which can also be cross-checked using different tracers toward the same cloud.

### 7. Conclusion

As one of the most versatile methods for probing the magnetic field in molecular clouds, the gradient method has been proposed to trace magnetic field orientations in multiple scenarios, including diffuse media, shocks, and self-gravitating regions. By examining the gradients of seven chemical tracers,



**Figure 11.** Statistical angle uncertainty (in degrees) in polarization data. (a) Polarization data used in comparison with the CO isotopologues data. (b) Polarization data used in comparison with the HCN, HNC, and HCO<sup>+</sup> data. (c) Polarization data used in comparison with the CS data.

and judging from the distribution of gradient vectors that are rotated by 90°, we present here an example making use of the recent advancement of gradient techniques from numerical and observational studies. Moreover, this work also suggests the promise of using multiple tracers with different tracing abilities to probe magnetic fields in different scales according to the density of the molecular clouds. We summarize as follows.

- 1. The VGT, which is for the first time applied to multiple tracers, is able to trace the variations in the plane-of-sky component of the magnetic field within different density regimes of the Vela C cloud.
- The VGT opens new a way of exploring the localized magnetic field in GMCs without the systematic uncertainty inherent in polarization observations associated with subtracting out foreground and background dust emission.
- 3. We see no column density threshold above which rerotation of the velocity gradients is required to match the BLASTPol inferred magnetic field orientation. This implies that, at the resolution of the Mopra data, we do not see the expected signature of the velocity gradients aligning parallel to the magnetic field in regions of gravitational collapse. We therefore infer that the collapsing regions constitute a small fraction of the Vela C cloud.

A.L. acknowledges the support of the NSF grant AST 1715754, and 1816234 as well as a distinguished visitor PVE/CAPES appointment at the Physics Graduate Program of the Federal University of Rio Grande do Norte, the INCT INEspao and Physics Graduate Program/UFRN. K.H.Y. acknowledges the support of the NSF grant AST 1816234. Y.H. acknowledges the support of the Future Generation Fellowship by Hu's family. L.M.F. is a Jansky Fellow of the National Radio Astronomy Observatory (NRAO). NRAO is a facility of the National Science Foundation (NSF operated under cooperative agreement by Associated Universities, Inc.). The Mopra radio telescope is part of the Australia Telescope National Facility, which is funded by the Australian Government for operation as a National Facility managed by CSIRO.

### Appendix Statistical Error in Polarization Data

We show the statistical angle uncertainty in polarization data in Figure 11. The errors are not constant across the BLASTPol map and the error is higher when it gets close to the boundary of Vela C. However, the mean error for the polarization data used in comparison with the CO isotopologues data is ~2.07, ~1.44 for that used for CS, and ~1.37 for that used for HCN, HNC, and HCO<sup>+</sup>. The statistical polarization angle errors depend on the signal to noise of the polarization fraction. For Gaussian polarization errors, the error  $\sigma_{\phi} \sim 28.6 \times \sigma_{p}/p$ , where  $\phi$  is the polarization angle and p is the polarization fraction (Fissel et al. 2016). Thus, for our polarization data, which is a  $3\sigma$  polarization detection, the statistical error is less than  $10^{\circ}$  (Fissel et al. 2019).

### **ORCID iDs**

Yue Hu https://orcid.org/0000-0002-8455-0805 Laura M. Fissel https://orcid.org/0000-0002-4666-609X P. A. Jones https://orcid.org/0000-0001-9429-9135 M. R. Cunningham https://orcid.org/0000-0001-7020-6176

#### References

```
Alves, F. O., Frau, P., Girart, J. M., et al. 2014, A&A, 569, L1
Andersson, B.-G., Lazarian, A., & Vaillancourt, J. E. 2015, ARA&A, 53, 501
Ballesteros-Paredes, J., Klessen, R. S., Mac Low, M.-M., &
   Vazquez-Semadeni, E. 2007, in Protostars and Planets V, ed. B. Reipurth,
   D. Jewitt, & K. Keil (Tucson, AZ: Univ. Arizona Press), 63
Bayet, E., Aladro, R., Martín, S., Viti, S., & Martín-Pintado, J. 2009, ApJ,
   707, 126
Bell, K. R., & Lin, D. N. C. 1994, ApJ, 427, 987
Bethell, T. J., Chepurnov, A., Lazarian, A., & Kim, J. 2007, ApJ, 663, 1055
Burkhart, B., Collins, D. C., & Lazarian, A. 2015, ApJ, 808, 48
Caprioli, D., & Spitkovsky, A. 2014, ApJ, 783, 91
Carilli, C. L., & Taylor, G. B. 2002, ARA&A, 40, 319
Chapman, N. L., Davidson, J. A., Goldsmith, P. F., et al. 2013, ApJ, 770, 151
Chen, C.-Y., Ostriker, E. C. & Classy Team 2015, AAS Meeting, 225, 110.02
Cho, J., & Lazarian, A. 2003, MNRAS, 345, 325
Cho, J., & Vishniac, E. T. 2000, ApJ, 539, 273
Clark, S. E., Peek, J. E. G., & Putman, M. E. 2014, ApJ, 789, 82
Cleeves, L. I., Bergin, E. A., Qi, C., Adams, F. C., & Öberg, K. I. 2015, ApJ,
   799, 204
Crutcher, R. M. 2012, ARA&A, 50, 29
Draine, B. T. 2011, Physics of the Interstellar and Intergalactic Medium
   (Princeton, NJ: Princeton Univ. Press)
Ellerbroek, L. E., Bik, A., Kaper, L., et al. 2013, A&A, 558, A102
Esquivel, A., & Lazarian, A. 2011, ApJ, 740, 117
Esquivel, A., Lazarian, A., & Pogosyan, D. 2015, ApJ, 814, 77
Fermi, E. 1949, PhRv, 75, 1169
Fissel, L. M., Ade, P. A. R., Angilè, F. E., et al. 2016, ApJ, 824, 134
Fissel, L. M., Ade, P. A. R., Angilè, F. E., et al. 2019, ApJ, 878, 110
Gao, Y., & Solomon, P. M. 2004, ApJ, 606, 271
Goldreich, P., & Sridhar, S. 1995, ApJ, 438, 763
González-Casanova, D. F., & Lazarian, A. 2017, ApJ, 835, 41
González-Casanova, D. F., Lazarian, A., & Burkhart, B. 2019, MNRAS,
```

483, 1287

```
Heitsch, F., Hartmann, L., Slyz, A. D., Devriendt, J. E. G., & Burkert, A. 2007,
   BAAS, 39, 887
Heyer, M., Gong, H., Ostriker, E., & Brunt, C. 2008, ApJ, 680, 420
Heyer, M., Krawczyk, C., Duval, J., & Jackson, J. M. 2009, ApJ, 699, 1092
HI4PI Collaboration, Ben Bekhti, N., Flöer, L., et al. 2016, A&A, 594, A116
Higdon, J. C. 1984, ApJ, 285, 109
Hill, A. S., Mao, S. A., Benjamin, R. A., Lockman, F. J., &
   McClure-Griffiths, N. M. 2013, ApJ, 777, 55
Hill, T., Motte, F., Didelon, P., et al. 2011, A&A, 533, A94
Hopkins, P. F., Quataert, E., & Murray, N. 2012, MNRAS, 421, 3522
Hsieh, C.-H., Hu, Y., Lai, S.-P., et al. 2019, ApJ, 873, 16
Hu, Y., Yuen, K. H., & Lazarian, A. 2018, MNRAS, 480, 1333
Hu, Y., Yuen, K. H., Lazarian, V., et al. 2019a, NatAs, 3, 776
Hu, Y., Yuen, K. H., & Lazarian, A. 2019b, arXiv:1908.09488
Heyer, M., Gong, H., Ostriker, E., & Brunt, C. 2008, ApJ, 680, 420
Jansson, R., & Farrar, G. R. 2012, ApJ, 757, 14
Kandel, D., Lazarian, A., & Pogosyan, D. 2016, MNRAS, 461, 1227
Kandel, D., Lazarian, A., & Pogosyan, D. 2017a, MNRAS, 464, 3617
Kandel, D., Lazarian, A., & Pogosyan, D. 2017b, MNRAS, 470, 3103
Lazarian, A. 2007, JQSRT, 106, 225
Lazarian, A., & Hoang, T. 2007, MNRAS, 378, 910
Lazarian, A., & Pogosyan, D. 2000, ApJ, 537, 720
Lazarian, A., Pogosyan, D., & Esquivel, A. 2002, in ASP Conf. Ser. 276,
   Seeing Through the Dust: The Detection of HI and the Exploration of the
  ISM in Galaxies, ed. A. R. Taylor, T. L. Landecker, & A. G. Willis (San
   Francisco, CA: ASP), 182
Lazarian, A., & Vishniac, E. T. 1999, ApJ, 517, 700
Lazarian, A., & Yuen, K. H. 2018a, ApJ, 865, 59
Lazarian, A., & Yuen, K. H. 2018b, ApJ, 853, 96
Lazarian, A., Yuen, K. H., Ho, K. W., et al. 2018, ApJ, 865, 46
```

Lazarian, A., Yuen, K. H., Lee, H., & Cho, J. 2017, ApJ, 842, 30

```
Leroy, A. K., Walter, F., Brinks, E., et al. 2008, AJ, 136, 2782
Li, H., Griffin, G. S., Krejny, M., et al. 2005, BAAS, 37, 1422
Mac Low, M.-M., & Klessen, R. S. 2004, RvMP, 76, 125
Maron, J., & Goldreich, P. 2001, ApJ, 554, 1175
Montgomery, D., & Matthaeus, W. H. 1995, ApJ, 447, 706
Murray, N., Quataert, E., & Thompson, T. A. 2010, ApJ, 709, 191
Netterfield, C. B., Ade, P. A. R., Bock, J. J., et al. 2009, ApJ, 707, 1824
Nguyen, H., Nguyen Lu'o'ng, Q., Martin, P. G., et al. 2015, ApJ, 812, 7
Ostriker, E. C., Stone, J. M., & Gammie, C. F. 2001, ApJ, 546, 980
Pety, J., Guzmán, V. V., Orkisz, J. H., et al. 2017, A&A, 599, A98
Planck Collaboration, Ade, P. A. R., Aghanim, N., et al. 2015, A&A,
  576, A106
Ridge, N. A., Di Francesco, J., Kirk, H., et al. 2006, AJ, 131, 2921
Seifried, D., Walch, S., Reissl, S., & Ibáñez-Mejía, J. C. 2019, MNRAS,
  482, 2697
Shebalin, J. V., Matthaeus, W. H., & Montgomery, D. 1983, JPIPh, 29, 525
Shirley, Y. L. 2015, PASP, 127, 299
Soler, J. D., Ade, P. A. R., Angilè, F. E., et al. 2017, A&A, 603, A64
Soler, J. D., & Hennebelle, P. 2017, A&A, 607, A2
Solomon, P. M., & Sage, L. J. 1988, ApJ, 334, 613
Stolle, C., Lühr, H., Rother, M., & Balasis, G. 2006, JGRA, 111, A02304
Turner, B. E., Pirogov, L., & Minh, Y. C. 1997, ApJ, 483, 235
Vollmer, B., Gratier, P., Braine, J., & Bot, C. 2017, A&A, 602, A51
Whittet, D. C. B., Hough, J. H., Lazarian, A., & Hoang, T. 2008, ApJ, 674, 304
Williams, J. P., de Geus, E. J., & Blitz, L. 1994, ApJ, 428, 693
Yamaguchi, N., Mizuno, N., Saito, H., et al. 1999, PASJ, 51, 775
Yuen, K. H., Chen, J., Hu, Y., et al. 2018, ApJ, 865, 54
Yuen, K. H., Hu, Y., Lazarian, A., & Pogosyan, D. 2019, arXiv:1904.03173
Yuen, K. H., & Lazarian, A. 2017a, ApJL, 837, L24
Yuen, K. H., & Lazarian, A. 2017b, arXiv:1703.03026
Zhang, J.-F., Lazarian, A., Ho, K. W., et al. 2019, MNRAS, 486, 4813
```